INCREMENTAL RNN: A DYNAMICAL VIEW.

Anonymous authors
Paper under double-blind review

ABSTRACT

Recurrent neural networks (RNNs) are particularly well-suited for modeling long-term dependencies in sequential data, but are notoriously hard to train because the error backpropagated in time either vanishes or explodes at an exponential rate. While a number of works attempt to mitigate this effect through gated recurrent units, skip-connections, parametric constraints and design choices, we propose a novel incremental RNN (iRNN), where hidden state vectors keep track of incremental changes, and as such approximate state-vector increments of Rosenblatt's (1962) continuous-time RNNs. iRNN exhibits identity gradients and is able to account for long-term dependencies (LTD). We show that our method is computationally efficient overcoming overheads of many existing methods that attempt to improve RNN training, while suffering no performance degradation. We demonstrate the utility of our approach with extensive experiments and show competitive performance against standard LSTMs on LTD and other non-LTD tasks.

1 INTRODUCTION

Recurrent neural networks (RNNs) in each round store a hidden state vector, $h_k \in \mathbb{R}^D$, and upon receiving the input vector, $x_{k+1} \in \mathbb{R}^d$, linearly transform the tuple (h_k, x_{k+1}) and pass it through a memoryless non-linearity to update the state over T rounds. Subsequently, RNNs output an affine function of the hidden states as its prediction. The model parameters (state/input/prediction parameters) are learnt by minimizing an empirical loss. This seemingly simple update rule has had significant success in learning complex patterns for sequential input data.

Nevertheless, that training RNNs can be challenging, and that performance can be uneven on tasks that require long-term-dependency (LTD), was first noted by Bengio et al. (1994) and later by other researchers. Pascanu et al. (2013b) attributed this to the fact that the error gradient back-propagated in time (BPTT), for the time-step k, is dominated by product of partials of hidden-state vectors, $\prod_{j=k}^{T-1} \frac{\partial h_{j+1}}{\partial h_j}$, and these products typically exhibit exponentially vanishing decay or explosion, resulting in incorrect credit assignment during training and test-time.

Rosenblatt (1962), on whose work we draw inspiration from, introduced continuous-time RNN (CTRNN) to mimic activation propagation in neural circuitry. CTRNN dynamics evolves as follows:

$$\tau \dot{g}(t) = -\alpha g(t) + \phi(Ug(t) + Wx(t) + b), \, t \geq t_0. \tag{1}$$

Here, $x(t) \in \mathbb{R}^d$ is the input signal, $g(t) \in \mathbb{R}^D$ is the hidden state vector of D neurons, $\dot{g}_i(t)$ is the rate of change of the i-th state component; $\tau \in \mathbb{R}^+$, referred to as the post-synaptic time-constant, impacts the rate of a neuron's response to the instantaneous activation $\phi(Ug(t) + Wx(t) + b)$; and $U \in \mathbb{R}^{D \times D}$, $W \in \mathbb{R}^{D \times d}$, $b \in \mathbb{R}^D$ are model parameters. In passing, note that recent RNN works that draw inspiration from ODE's (Chang et al., 2019) are special cases of CTRNN ($\tau = 1$, $\alpha = 0$).

Vanishing Gradients. The qualitative aspects of the CTRNN dynamics is transparent in its integral form:

$$g(t) = e^{-\alpha \frac{t-t_0}{\tau}} g(t_0) + \frac{1}{\tau} \int_{t_0}^t e^{-\alpha \frac{t-s}{\tau}} \phi(Ug(s) + Wx(s) + b)ds \tag{2}$$

This integral form reveals that the partials of hidden-state vector with respect to the initial condition, $\frac{\partial g(t)}{\partial g(t_0)}$, gets attenuated rapidly (first term in RHS), and so we face a vanishing gradient problem. We will address this issue later but we note that this is not an artifact of CTRNN but is exhibited by ODEs that have motivated other RNNs (see Sec. 2).

Shannon-Nyquist Sampling. A key property of CTRNN is that the time-constant τ together with the first term $-g(t)$, is in effect a low-pass filter with bandwidth $\alpha\tau^{-1}$ suppressing high frequency components of the activation signal, $\phi((Ug(s)) + (Wx(s)) + b)$. This is good, because, by virtue of the Shannon-Nyquist sampling theorem, we can now *maintain fidelity* of discrete samples with respect to continuous time dynamics, in contrast to conventional ODEs ($\alpha = 0$). Additionally, since high-frequencies are already suppressed, in effect we may assume that the input signal $x(t)$ is slowly varying relative to the post-synaptic time constant τ.

Equilibrium. The combination of low pass filtering and slowly time varying input has a significant bearing. The state vector as well as the discrete samples evolve close to the equilibrium state, i.e., $g(t) \approx \phi(Ug(t) + Wx(t) + b)$ under general conditions (Sec. 3).

Incremental Updates. Whether or not system is in equilibrium, the integral form in Eq. 2 points to gradient attenuation as a fundamental issue. To overcome this situation, we store and process increments rather than the cumulative values $g(t)$ and propose dynamic evolution in terms of increments. Let us denote hidden state sequence as $h_k \in \mathbb{R}^D$ and input sequence $x_k \in \mathbb{R}^d$. For $k = 1, 2, \ldots, T$, and a suitable $\beta > 0$

$$\tau \dot{g}(t) = -\alpha(g(t) \pm h_{k-1}) + \phi(U(g(t) \pm h_{k-1}) + Wx_k + b), \, g(0) = 0, \, t \geq 0 \qquad (3)$$
$$h_k^{\beta \cdot \tau} \triangleq g(\beta \cdot \tau)$$

Incremental RNN (iRNN) achieves Identity Gradient. We propose to discretize Eq. 3 to realize iRNN (see Sec. 3). In round k, it takes the previous state $h_{k-1} \in \mathbb{R}^D$ and input $x_k \in \mathbb{R}^d$ and outputs $h_k \in \mathbb{R}^D$ after simulating the CTRNN evolution in discrete-time, for a suitable number of discrete steps. We show that the proposed RNN approximates the continuous dynamics and solves the vanishing/exploding gradient issue by ensuring identity gradient[1]. In general, we consider two options, SiRNN, whose state is updated with a single CTRNN sample, similar to vanilla RNNs, and, iRNN, with many intermediate samples. SiRNN is well-suited for slowly varying inputs.

Contributions. To summarize, we list our main contributions:
(A) iRNN converges to equilibrium for typical activation functions. The partial gradients of hidden-state vectors for iRNNs converge to identity, thus solving vanishing/exploding gradient problem!
(B) iRNN converges rapidly, at an exponential rate in the number of discrete samplings of Eq. 1. SiRNN, the single-step iRNN, is efficient and can be leveraged for slowly varying input sequences. It exhibits fast training time, has fewer parameters and better accuracy relative to standard LSTMs.
(C) Extensive experiments on LTD datasets show that we improve upon standard LSTM accuracy as well as other recent proposals that are based on designing transition matrices and/or skip connections. iRNNs/SiRNNs are robust to time-series distortions such as noise paddings
(D) While our method extends directly (see Appendix A.1) to Deep RNNs, we deem these extensions complementary, and focus on single-layer to highlight our incremental perspective.

2 RELATED WORK

Gated Architectures. Long short-term memory (LSTM) (Hochreiter & Schmidhuber, 1997) is widely used in RNNs to model long-term dependency in sequential data. Gated recurrent unit (GRU) (Cho et al., 2014) is another gating mechanism that has been demonstrated to achieve similar performance of LSTM with fewer parameters. Some recent gated RNNs include UGRNN (Collins et al., 2016), and FastGRNN (Kusupati et al., 2018). While mitigating vanishing/exploding gradients, they do not eliminate it. Often, these models incur increased inference, training costs, and model size.

Unitary RNNs. Arjovsky et al. (2016); Jing et al. (2017); Zhang et al. (2018); Mhammedi et al. (2016) focus on designing well-conditioned state transition matrices, attempting to enforce unitary-property, during training. Unitary property does not generally circumvent vanishing gradient (Pennington et al. (2017)). Also, it limits expressive power and prediction accuracy while also increasing training time.

Deep RNNs. These are nonlinear transition functions incorporated into RNNs for performance improvement. For instance, Pascanu et al. (2013a) empirically analyzed the problem of how to

---

[1]**Does this imply infinite input recall and poor generalization?**. No. Models such as $h_k = h_{k-1}$ and $h_k = h_{k-1} + Wx_k$ have identity gradient but cannot recall inputs. iRNNs state-vector responds to changes in input. As such it cannot recall.

construct deep RNNs. Zilly et al. (2017) proposed extending the LSTM architecture to allow step-to-step transition depths larger than one. Mujika et al. (2017) proposed incorporating the strengths of both multiscale RNNs and deep transition RNNs to learn complex transition functions from one timestep to the next. While Deep RNNs offer richer representations relative to single-layers, it is complementary to iRNNs.

Residual/Skip Connections. Jaeger et al. (2007); Bengio et al. (2013); Chang et al. (2017); Campos et al. (2017); Kusupati et al. (2018) feed-forward state vectors to induce skip or residual connections, to serve as a middle ground between feed-forward and recurrent models, and to mitigate gradient decay. Nevertheless, these connections, cannot entirely eliminate gradient explosion/decay. For instance, Kusupati et al. (2018) suggest $h_k = \alpha h_k + \beta \phi(U h_{k-1} + W x_k + b)$, and tune $\alpha \approx 1$ and $\beta \approx 1 - \alpha$, while realizing near identity gradient can conflict with good accuracy, as also observed in our experiments.

Linear RNNs. (Bradbury et al., 2016; Lei et al., 2018; Balduzzi & Ghifary, 2016) have focused on speeding up recurrent neural networks by replacing recurrent connections, such as hidden-to-hidden interactions, with light weight linear components. While this has led to reduced training time, it has resulted in significantly increasing model size. For example, Lei et al. (2018) typically requires twice the number of cells for LSTM level performance.

ODE/Dynamical Perspective. There are a few works that draw inspiration from ODEs, and attempt to address training stability, but in the end do not eliminate vanishing/exploding gradients. Talathi & Vartak (2015) proposed a modified weight initialization strategy based on a simple dynamical system perspective on weight initialization process that leads to successfully training RNNs composed of ReLUs. Niu et al. (2019) analyzed RNN architectures using numerical methods of ODE and propose a family of ODE-RNNs. Chang et al. (2019), propose Antisymmetric-RNN. Their key idea is to express the transition matrix in Eq. 1, for the special case $\alpha = 0, \tau = 1$, as a difference: $U = V - V^T$ and note that the eigenspectrum is imaginary. Nevertheless, Euler discretization, in this context leads to instability, necessitating damping of the system, and as such vanishing gradient cannot be completely eliminated. Its behavior is analogous to FastRNN Kusupati et al. (2018), in that, identity gradient conflicts with high accuracy. In summary, we are the first to propose evolution over the equilibrium manifold, and demonstrating identity gradients.

3 METHOD

We use Euler's method to discretize Eq. 3 in steps $\delta = \eta \tau$. Denoting the ith step as $g_i = g(i\delta)$

$$\tau \frac{g_i - g_{i-1}}{\delta} = -\alpha(g_{i-1} + h_{k-1}) + \phi(U(g_{i-1} + h_{k-1}) + W x_k + b), \ g_0 = 0, \ i \in [K] \quad (4)$$

Rearranging terms we get a compact form for IRNN. We run the recursion for $i \in [K]$ with $g_0 = 0$. We generalize the method and allow tuning parameters, η to depend on step i and round k η_k^i

$$g_i = g_{i-1} + \eta_k^i(\phi(U(g_{i-1} + h_{k-1}) + W x_k + b) - \alpha(g_{i-1} + h_{k-1})) \quad (5)$$
$$h_k^K = g_K$$

In many of our examples, we find the input sequence is indeed slowly varying, and $K = 1$ is often sufficient. We refer to this as single-step-incremental-RNN (SiRNN) and drop the superscript $K = 1$,

$$h_k = \eta_k(\phi(U(h_{k-1}) + W x_k + b) - \alpha h_{k-1}) \quad (6)$$

We learn parameters, U, W, b and any additional parameters in the loss function, ν_k by solving an empirical risk minimization problem, in a conventional manner, using back-propagation.

Implementation: Such update rules can be efficiently implemented using networks, as illustrated in Fig. 1, where $\oplus, \ominus$ denote the entry-wise plus and minus operators, and each square denotes a learnable parameter or function with parameters of the network. Once K is fixed, iRNN can be readily converted into feedforward network leveraging the blocks of Fig. 1.
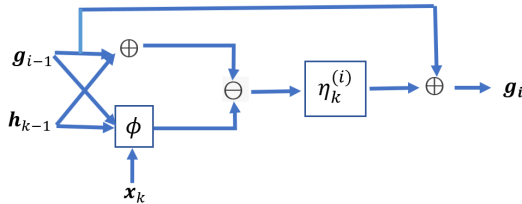

Figure 1: iRNN Block Implementation as a feedforward block.

3.1 Identity Gradient Property and Convergence Guarantees.

Let us now collect a few properties of Eq. 3 and Eq. 5. First, denote the equilibrium solutions for an arbitrary input $x \in \mathbb{R}^d$, arbitrary state-vector $\nu \in \mathbb{R}^D$, in an arbitrary round:

$$\mathcal{M}_{eq}(x, \nu) = \{\mu \in \mathbb{R}^D \mid \alpha(\mu + \nu) = \phi(U(\mu + \nu) + Wx + b)\}$$

Whenever the equilibrium set is a singleton, we denote it as a function $h_{eq}(x, \nu)$. For simplicity, we assume below that η_k^i is a positive constant independent of k and i.

Proposition 1. *Suppose, $\phi(\cdot)$ is a 1-Lipshitz function in the norm induced by $\|\cdot\|$, and $\|U\| < \alpha$, then for any $x_k \in \mathbb{R}^d$ and $h_{k-1} \in \mathbb{R}^D$, it follows that $\mathcal{M}_{eq}(x, \nu)$ is a singleton and as $K \to \infty$, the iRNN recursions converge to this solution, namely, $h_k = \lim_{K \to \infty} g_K = h_{eq}(x_k, h_{k-1})$*

Proof. Define $T : \mathbb{R}^D \to \mathbb{R}^d$, with $T(g) = (1 - \eta\alpha)g + \eta(\phi(U(g + h_{k-1}) + Wx_k + b) - h_{k-1})$. It follows that $T(\cdot)$ is a contraction:

$$\|T(g) - T(g')\| \leq (1 - \eta\alpha)\|g - g'\| + \eta\|\phi(U(g + h_{k-1}) + Wx_k + b) - \phi(U(g' + h_{k-1}) + Wx_k + b)\|$$
$$\leq (1 - \eta\alpha + \|U\|\eta)\|g - g'\| < \|g - g'\|.$$

We now invoke the Banach fixed point theorem, which asserts that a contractive operator on a complete metric space converges to a unique fixed point, namely, $T^K(g) \to g_*$. Upon substitution, we see that this point g_* must be such that, $\phi(U(g_* + h_{k-1}) + Wx_k + b) - (g_* + h_{k-1}) = 0$. Thus equilibrium point exists and is unique. Result follows by setting $h_k \triangleq h_{eq}(x_k, h_{k-1})$. □

Next we show for $\eta > 0$, iRNN converges at a linear rate, which follows directly from Proposition 1.

Proposition 2. *Under the setup in Proposition 1, it follows that,*

$$\|h_k^K - h_{eq}(x_k, h_{k-1})\| \leq (1 - \alpha\eta + \eta\|U\|)^K \|h_k^1 - h_{eq}(x_k, h_{k-1})\|$$

Remark. Prop. 1 accounts for typical activation functions ReLU, tanh, sigmoids as well as deep RNNs (appendix A.1).
Prop. 2 justifies SiRNN; if x_k is slowly varying, $h_k^1 \approx h_{eq}(x_k, h_{k-1})$ resulting in rapid convergence.

In passing we point out that, in our experiments, we learn parameters η_k^i, and a result that accounts for this case is desirable. We describe this case in Appendix A.2. A fundamental result we describe below is that partials of hidden-state vectors, on the equilibrium surface is unity. For technical simplicity, we assume a continuously differentiable activation, which appears to exclude ReLU activations. Nevertheless, we can overcome this issue, but requires more technical arguments. The main difficulty stems from ensuring that derivatives along the equilibrium surface exist, and this can be realized by invoking the implicit function theorem (IFT). IFT requires continuous differentiability, which ReLUs violate. Nevertheless, recent results [2] suggests that one can state implicit function theorem for everywhere differentiable functions, which includes ReLUs.

Theorem 1. *Suppose $\phi(\cdot)$ is a continuously differentiable, 1-Lipshitz function, with $\|U\| < \alpha$. Then as $K \to \infty$, $\frac{\partial h_k}{\partial h_{k-1}} \to \frac{\partial h_{eq}(x_k, h_{k-1})}{\partial h_{k-1}} = -I$. Furthermore, as $K \to \infty$ the partial gradients over arbitrary number of rounds for iRNN is identity.*

$$\frac{\partial h_m}{\partial h_n} = \prod_{m \geq k > n} \frac{\partial h_k}{\partial h_{k-1}} = (-1)^{m-n}\mathbf{I} \Rightarrow \left\|\frac{\partial h_m}{\partial h_n}\right\| = 1. \tag{7}$$

Proof. Define, $\psi(g, h_{k-1}) = \phi(U(g + h_{k-1}) + Wx_k + b) - \alpha(g + h_{k-1})$. We overload notation and view the equilibrium point as a function of h_{k-1}, i.e., $g_*(h_{k-1}) = h_{eq}(x_k, h_{k-1})$. Invoking standard results[3] in ODE's, it follows that $g_*(h_{k-1})$ is a smooth function, so long as the Jacobian, $\nabla_g \psi(g_*, h_{k-1})$ with respect to the first coordinate, g_*, is non-singular. Upon computation, we see that, $\nabla_g \phi(g_*, h_{k-1}) = \nabla\phi(g_*, h_{k-1})U - \alpha I$, is non-singular, since $\|\nabla\phi(g_*, h_{k-1})U\| < \|U\|$. It follows that we can take partials of the state-vectors. By taking the partial derivatives *w.r.t.* h_{k-1} in Eq. 5, at the equilibrium points we have $[\nabla\psi(g_*, h_{k-1}) - \alpha\mathbf{I}][\frac{\partial g_*}{\partial h_{k-1}} + \mathbf{I}] = \mathbf{0}$. The rest of the proof follows by observing that the first term is non-singular. □

---

[2]terrytao.wordpress.com/2011/09/12/the-inverse-function-theorem-for-everywhere-differentiable-maps/
[3]http://cosweb1.fau.edu/~jmirelesjames/ODE_course/lectureNotes_
shortVersion_day1.pdf

Remark. We notice that replacing h_{k-1} with $-h_{k-1}$ in Eq. 11 will lead to $\frac{\partial h_{eq}}{\partial h_{k-1}} = \mathbf{I}$, which also has no impact on magnitudes of gradients. As a result, both choices are suitable for circumventing vanishing or exploding gradients during training, but still may converge to different local minima and thus result in different test-time performance. Furthermore, notice that the norm preserving property is somewhat insensitive to choices of α, so long as the non-singular condition is satisfied.

Figure 2: Phase-space trajectory with tanh activation of RNN, FastRNN, iRNN. X-axis denotes 1st dimension, and Y-axis 2nd dimension of 2D hidden state subject to random walk input with variance 10 for 1000 time-steps. Parameters U, W, b are randomly initialized. RNN states are scaled to fit plot since FastRNN is not required to be in the cube.

3.2 iRNN Design Implications: Low-Rank Model Parametrization

Fig. 2 depicts phase portrait and illustrates salient differences between RNN, FastRNN (RNN with skip connection), and iRNN (K=5). RNN and FastRNN exhibit complex trajectories, while iRNN trajectory is smooth, projecting initial point (black circle) onto the equilibrium surface (blue) and moving within it (green). This suggests that iRNN trajectory belongs to a low-dimensional manifold.

Variation of Equilibrium *w.r.t.* Input. As before, h_{eq} be an equilibrium solution for some tuple (h_{k-1}, x_k). It follows that,

$$(\alpha\mathbf{I} - \nabla\phi(U(h_{eq} + \mathbf{h}_{k-1}) + Wx_k + b)U)\partial h_{eq} = \nabla\phi(U(h_{eq} + h_{k-1}) + Wx_k + b)W\partial x_k$$

This suggests that, whenever the input undergoes a slow variation, we expect that the equilibrium point moves in such a way that $U\partial h_{eq}$ must lie in a transformed span of W. Now $W \in \mathbb{R}^{D\times d}$ with $d \ll D$, which implies that $(\alpha\mathbf{I} - \nabla\phi(U(h_{eq} + h_{k-1}) + Wx_k + b)U$ is rank-deficient.

Low Rank Matrix Parameterization. For typical activation functions, note that whenever the argument is in the unsaturated regime, $\nabla\phi(\cdot) \approx \mathbf{I}$. We then approximately get $\text{span}(\alpha\mathbf{I} - U) \approx \text{span}(W)$. We can express these constraints as $U = \alpha\mathbf{I} + VH$ with low-rank matrices $V \in \mathbb{R}^{D\times d_1}, H \in \mathbb{R}^{d_1\times D}$, and further map both Uh_k and Wx_k onto a shared space. Since in our experiments the signal vectors we encounter are low-dimensional, and sequential inputs vary slowly over time, we enforce this restriction in all our experiments. In particular, we consider,

$$\phi\left(P[U(h_k^K + h_{k-1}) + Wx_k + b]\right) - (h_k^K + h_{k-1}) = \mathbf{0}. \tag{8}$$

The parameter matrix $P \in \mathbb{R}^{D\times D}$ maps the contributions from input and hidden states onto the same space. To decrease model-size we let $P = U = (\mathbf{I} + VH)$ learn these parameters.

4 Experiments

We organize this section as follows. First, the experimental setup, competing algorithms will be described. Then we present an ablative analysis to highlight salient aspects of iRNN and justify some of our experimental choices. We then plot and tabulate experimental results on benchmark datasets.

4.1 Experimental Setup and Baselines

Choice of Competing Methods: We choose competing methods based on the following criteria: (a) methods that are devoid of additional application or dataset-specific heuristics, (b) methods that leverage only single cell/block/layer, and (c) methods without the benefit of complementary add-ons (such as gating, advanced regularization, model compression, etc.). Requiring (a) is not controversial since our goal is methodological. Conditions (b),(c) are justifiable since we could also leverage these add-ons and are not germane to any particular method[4]. We benchmark *iRNN* against standard RNN, LSTM (Hochreiter & Schmidhuber, 1997), (ungated) AntisymmetricRNN (Chang et al., 2019), (ungated) FastRNN (Kusupati et al., 2018).
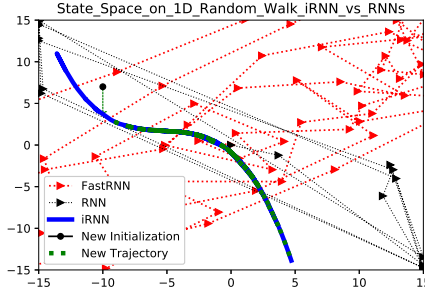

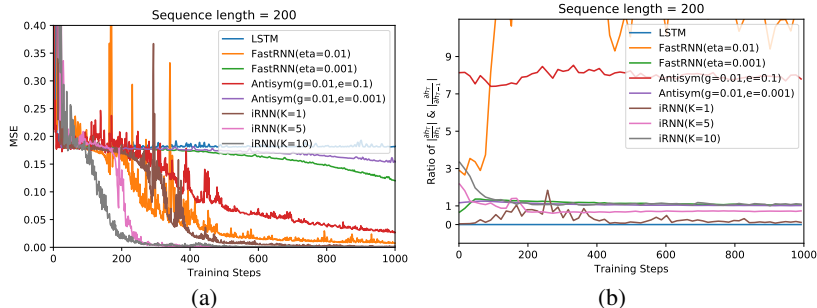[4]These conditions eliminate some potential baselines. We provide specific justifications in the appendix A.4.

Figure 3: Exploratory experiments for the Add task (a) Convergence with varying K; (b) Ratio $\|\frac{\partial h_T}{\partial h_1}\|/\|\frac{\partial h_T}{\partial h_{T-1}}\|$ illustrates Vanishing/Exploding gradient ($\|\frac{\partial h_T}{\partial h_{T-1}}\|$ and loss gradients are omitted but displayed in A.6.8. For iRNN (a) and (b) together show strong correlation of gradient with accuracy in contrast to other methods.

Unitary RNN Variants. Results for methods based on unitary transitions (such as Arjovsky et al. (2016); Wisdom et al. (2016); Vorontsov et al. (2017); Zhang et al. (2018)) are not reported in the main paper (when available reported in appendix) for the following reasons: (a) They are substantially more expensive, and requiring large model sizes; (b) Apart from the benchmark copy and add tasks, results tabulated by FastRNN and Antisymmetric authors (see Zhang et al. (2018); Chang et al. (2019)) show that they are well below SOTA; (c) iRNN dominates unitary-RNN variants on add-task (see Sec. 4.3.1); (d) On copy task, while unitary invariants are superior, Vorontsov et al. (2017) attributes it to modReLU or leaky ReLU activations. Leaky ReLUs allow for linear transitions, and copy task being a memory task benefits from it. With hard non-linear activation, unitary RNN variants can take up to 1000's of epochs for even 100-length sequences (Vorontsov et al. (2017)).

Implementation. For all our experiments, we used the parametrized update formulation in Eq. 8 for *iRNN* . We used tensorflow framework for our experiments. For most competing methods apart from AntisymmetricRNN, which we implemented, code is publicly available. All the experiments were run on an Nvidia GTX 1080 GPU with CUDA 9 and cuDNN 7.0 on a machine with Intel Xeon 2.60 GHz CPU with 20 cores.

Datasets. Pre-processing and feature extraction details for all publicly available datasets are in the appendix A.3. We replicate benchmark test/train split with 20% of training data for validation to tune hyperparameters. Reported results are based on the full training set, and performance achieved on the publicly available test set. Table 4 (Appendix) and A.3 describes details for all the data sets.

Hyper Parameters We used grid search and fine-grained validation wherever possible to set the hyper-parameters of each algorithm, or according to the settings published in (Kusupati et al., 2018; Arjovsky et al., 2016) (*e.g.* number of hidden states). Both the learning rate and η's were initialized to 10^{-2}. The batch size of 128 seems to work well across all the data sets. We used ReLU as the non-linearity and Adam (Kingma & Ba (2015)) as the optimizer for all the experiments.

4.2 ABLATIVE ANALYSIS

We perform ablative analysis on the benchmark add-task (Sec 4.3.1) for sequence length 200 for 1000 iterations and explore mean-squared error as a metric. Fig. 3 depicts salient results.

(a) Identity Gradients & Accuracy: iRNN accuracy is correlated with identity gradients. Increasing K improves gradients, and correlates with increased accuracy (Fig. 3). While other models $h_t = \alpha h_{t-1} + \beta \phi((U - \gamma I)h_{t-1} + W x_t)$, can realize identity gradients for suitable choices; linear ($\alpha = 1, \beta = 1, \gamma = 0, U = 0$), FastRNN ($\alpha \approx 1, \beta \approx 0, \gamma = 0$) and Antisymmetric ($\alpha = 1, \beta = 1, U = V - V^T, \|U\| \leq \gamma$), this goal may not be correlated with improved test accuracy. FastRNN($\eta = 0.001$), Antisymmetric ($\gamma = 0.01, \epsilon = 0.001$) have good gradients but poorer test accuracy relative to FastRNN($\eta = 0.01$), Antisymmetric($\gamma = 0.01, \epsilon = 0.1$), with poorer gradients.

(b) Identity gradient implies faster convergence: Identity gradient, whenever effective, must be capable of assigning credit to the informative parts, which in turn results in larger loss gradients, and significantly faster convergence with number of iterations. This is borne out in figure 3(a). iRNN for larger K is closer to identity gradient with fewer (unstable) spikes ($K = 1, 5, 10$). With $K = 10$, iRNN converges within 300 iterations while competing methods take about twice this time (other baselines not included here exhibited poorer performance than the once plotted).
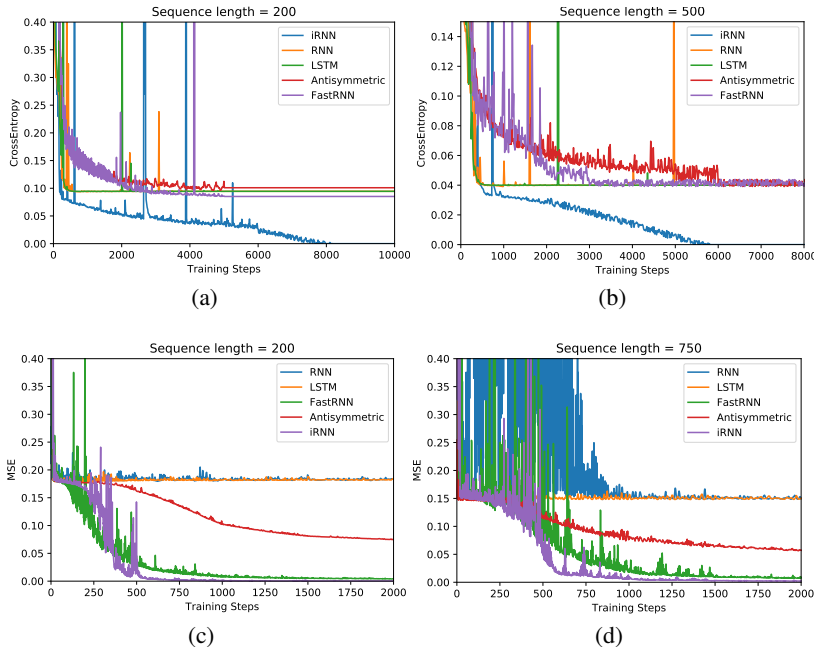
Figure 4: Following Arjovsky et al. (2016) we display average Cross Entropy for the Copy Task (Sequence Length (with baseline memoryless strategy)): (a) 200 (0.09) (b) 500 (0.039). Mean Squared Error for the Add Task, baseline performance is 0.167 (Sequence Length) : (c) 200 (d) 750

(c) SiRNN (iRNN with $K = 1$ is generally sufficient). Fig. 3(a) illustrates that iRNN $K = \{5, 10\}$ achieves slightly faster convergence than SiRNN, but the computational overhead per iteration roughly doubles or triples in comparison. Nevertheless, SiRNN is faster relative to competitors. For this reason, we only tabulate SiRNN, whenever it is SOTA in a benchmark experiments.

4.3 LONG-TERM DEPENDENCY AND OTHER TASKS

We list five types of datasets, all of which in some way require effective gradient propagation: (1) Conventional Benchmark LTD tasks (Add & Copy tasks) that illustrate that iRNN can rapidly learn long-term dependence; (2) Benchmark vision tasks (pixel MNIST, perm-MNIST) that may not require long-term, but nevertheless, demonstrates that *iRNN* achieves SOTA for short term dependencies but with less resources. (3) Noise Padded (LTD) Vision tasks (Noisy MNIST, Noisy CIFAR), where a large noise time segment separates information segments and the terminal state, and so the learner must extract information parts while rejecting the noisy parts; (4) short duration activity embedded in a larger time-window (HAR-2, Google-30 in Appendix Table 4 and many others A.6), that usually arise in the context of smart IoT applications and require a small model-size footprint. Chang et al. (2019) further justify (3) and (4) as LTD, because for these datasets where only a smaller unknown segment(s) of a longer sequence is informative. (5) Sequence-sequence prediction tasks (PTB language modeling) that are different from terminal prediction (reported in appendix A.6).

4.3.1 STANDARD BENCHMARK LTD TASKS : ADDITION & COPY MEMORY

Addition and Copy tasks (Hochreiter & Schmidhuber, 1997) have long been used as benchmarks in the literature to evaluate LTD (Hori et al., 2017; Zhang et al., 2018; Arjovsky et al., 2016; Martens & Sutskever, 2011). We follow the setup described in Arjovsky et al. (2016) to create the adding and copying tasks. See appendix A.3 for detailed description.

Figure 4 show the average performance of various methods on these tasks. For the copying task we observe that *iRNN* converges rapidly to the naive baseline and is the only method to achieve zero average cross entropy. For the addition task, both FastRNN and *iRNN* solves the addition task but FastRNN takes twice the number of iterations to reach desired 0 MSE. [5] In both the tasks,

---

[5] Note that LSTM solves the addition problem in Arjovsky et al. (2016) only with more than $10k$ iterations. We only use $2k$ iterations in our experiments to demonstrate the effectiveness of our method.

iRNN performance is much more stable across number of online training samples. In contrast, other methods either takes a lot of samples to match *iRNN* 's performance or depict high variance in the evaluation metric. This shows that *iRNN* converges faster than the baselines (to the desired error). *These results demonstrate that* iRNN *easily and quickly learns the long term dependencies* . We omitted reporting unitary RNN variants for Add and Copy task. See Sec. 4.1 for copy task. On Add-task we point out that our performance is superior. In particular, for the longer $T = 750$ length, Arjovsky et al. (2016), points out that MSE does not reach zero, and uRNN is noisy. Others either (Wisdom et al., 2016) do not report add-task or report only for shorter lengths (Zhang et al., 2018).

Table 1: Results for Pixel-by-Pixel MNIST and Permuted MNIST datasets. K denotes pre-defined recursions embedded in graph to reach equilibrium.

Data set	Algorithm	Accuracy (%)	Train Time (hr)	#Params
Pixel-MNIST	FastRNN	96.44	15.10	33k
	RNN	94.10	45.56	14k
	LSTM	97.81	26.57	53k
	Antisymmetric	98.01	8.61	14k
	iRNN (K=1)	97.73	**2.83**	**4k**
	***iRNN* (K=3)**	**98.13**	2.93	**4k**
Permute-MNIST	FastRNN	92.68	9.32	8.75k
	LSTM	92.61	19.31	35k
	Antisymmetric	93.59	4.75	14k
	***iRNN* (K=1)**	**95.62**	**2.41**	**8k**

4.3.2 NON LTD VISION TASKS: PIXEL MNIST, PERMUTE MNIST

Next, we perform experiments on the sequential vision tasks: (a) classification of MNIST images on a pixel-by-pixel sequence; (b) a fixed random permuted MNIST sequence (Lecun et al., 1998). These tasks typically do not fall in the LTD categories (Chang et al., 2019), but are useful to demonstrate faster training, which can be attributed to better gradients.

For the pixel-MNIST task, Kusupati et al. (2018) reports that it takes significantly longer time for existing (LSTMs, Unitary, Gated, Spectral) RNNs to converge to reasonable performance. In contrast, FastRNN trains at least $2x$ faster than LSTMs. Our results (table 1) for *iRNN* shows a $9x$ speedup relative LSTMs, and $2x$ speedup in comparison to Antisymmetric. In terms of test accuracy, *iRNN* matches the performance of Antisymmetric, but with at least $3x$ fewer parameters. We did not gain much with increased K values[6]. For the permuted version of this task, we seem to outperform the existing baselines [7]. In both tasks, *iRNN* trained at least $2x$ faster than the strongest baselines. *These results demonstrate that* iRNN *converges much faster than the baselines with fewer parameters.*

4.3.3 NOISE PADDING TASKS: NOISY-MNIST, NOISY-CIFAR

Additionally, as in Chang et al. (2019), we *induce* LTD by padding CIFAR-10 with noise exactly replicating their setup, resulting in Noisy-CIFAR. We extend this setting to MNIST dataset resulting in Noisy-MNIST. Intuitively we expect our model to be resilient to such perturbations. We attribute iRNN's superior performance to the fact that it is capable of suppressing noise. For example, say noise is padded at $t > \tau$ and this results in Wx_t being zero on average. For *iRNN* the resulting states ceases to be updated. So *iRNN* recalls last informative state h_τ (modulo const) unlike RNNs/variants! Thus information from signal component is possibly better preserved.

Results for Noisy-MNIST and Noisy-CIFAR are shown in Table 2. Note that almost all timesteps contain noise in these datasets. LSTMs perform poorly on these tasks due to vanishing gradients. This

---

[6] For some existing comparisons LSTM have achieved roughly 98.9 with dataset specific heuristics (Cooijmans et al., 2016), but we could not achieve this performance in our comparison (and so have many others like (Kusupati et al., 2018; Zhang et al., 2018; Arjovsky et al., 2016)).

[7] Note that there's no standard permutation in the literature. This may be the main reason we could not replicate Chang et al. (2019) performance on the permute MNIST task.

Table 2: Results for Noise Padded CIFAR-10 and MNIST datasets. Since the equilibrium surface is smooth and resilient to small perturbations, *iRNN* achieves better performance than the baselines with faster convergence.

Data set	Algorithm	Accuracy (%)	Train Time (hr)	#Params
Noisy-MNIST	FastRNN	98.12	8.93	11k
	LSTM	10.31	19.43	44k
	Antisymmetric	97.76	5.21	10k
	iRNN **(K=1)**	**98.48**	**2.39**	**6k**
Noisy-CIFAR	FastRNN	45.76	11.61	16k
	LSTM	11.60	23.47	64k
	Antisymmetric	48.63	5.81	16k
	iRNN **(K=1)**	**54.50**	**2.47**	**11.5k**

is consistent with the earlier observations (Chang et al., 2019). *iRNN* outperforms the baselines very comprehensively on CIFAR-10, while on MNIST the gains are smaller, as it's a relatively easier task. *These results show that* iRNN *is more resilient to noise and can account for longer dependencies.*

Table 3: Results for Activity Recognition Datasets. *iRNN* outperforms the baselines on all metrics even with $K = 1$. Its worth noticing that although $K = 5$ increases test time, it's well within LSTM's numbers, the overall train time and resulting performance are better than $K = 1$.

Data set	Algorithm	Accuracy (%)	Train Time (hr)	#Params	Test Time (ms)
HAR-2	FastRNN	94.50	0.063	7.5k	**0.01**
	RNN	91.31	0.114	7.5k	**0.01**
	LSTM	93.65	0.183	16k	0.04
	Antisymmetric	93.15	0.087	7.5k	**0.01**
	iRNN (K=1)	95.32	0.061	**4k**	**0.01**
	iRNN **(K=5)**	**96.30**	**0.018**	**4k**	0.03
Google-30	FastRNN	91.60	1.30	18k	**0.01**
	RNN	80.05	2.13	12k	**0.01**
	LSTM	90.31	2.63	41k	0.05
	Antisymmetric	90.91	0.54	12k	**0.01**
	iRNN (K=1)	93.77	**0.44**	**8.5k**	**0.01**
	iRNN **(K=5)**	**94.23**	**0.44**	**8.5k**	0.05

4.3.4 SHORT DURATION EMBEDDED ACTIVITY RECOGNITION TASKS: HAR-2, GOOGLE-30

We are interested in detecting activity embedded in a longer sequence with small footprint RNNs (Kusupati et al. (2018)): (a) Google-30 (Warden, 2018), *i.e.* detection of utterances of 30 commands plus background noise and silence, and (b) HAR-2 (Anguita et al., 2012), *i.e.* Human Activity Recognition from an accelerometer and gyroscope on a Samsung Galaxy S3 smartphone.

Table 3 shows accuracy, training time, number of parameters and prediction time. Even with $K = 1$, we compare well against competing methods, and iRNN accuracy improves with larger K. Interestingly, higher K yields faster training as well as moderate prediction time, despite the overhead of additional recursions. *These results show that* iRNN *outperforms baselines on activity recognition tasks, and fits within IoT/edge-device budgets.*

5 CONCLUSION

Drawing inspiration from Rosenblatts Continuous RNNs, we developed discrete time incremental RNN (iRNN). Leveraging equilibrium properties of CTRNN, iRNN solves exploding/vanishing gradient problem. We show that iRNN improved gradients are directly correlated with improved test accuracy. A number of experiments demonstrate iRNNs responsiveness to long-term dependency tasks. In addition, due to its smooth low-dimensional trajectories, it has a lightweight footprint that can be leveraged for IoT applications.

REFERENCES

Kerem Altun, Billur Barshan, and Orkun Tunçel. Comparative study on classifying human activities with miniature inertial and magnetic sensors. *Pattern Recogn.*, 43(10):3605–3620, October 2010. ISSN 0031-3203. doi: 10.1016/j.patcog.2010.04.019. URL `http://dx.doi.org/10.1016/j.patcog.2010.04.019`.

Davide Anguita, Alessandro Ghio, Luca Oneto, Xavier Parra, and Jorge L. Reyes-Ortiz. Human activity recognition on smartphones using a multiclass hardware-friendly support vector machine. In *Proceedings of the 4th International Conference on Ambient Assisted Living and Home Care*, IWAAL'12, pp. 216–223, Berlin, Heidelberg, 2012. Springer-Verlag. ISBN 978-3-642-35394-9. doi: 10.1007/978-3-642-35395-6_30. URL `http://dx.doi.org/10.1007/978-3-642-35395-6_30`.

Martin Arjovsky, Amar Shah, and Yoshua Bengio. Unitary evolution recurrent neural networks. In *International Conference on Machine Learning*, pp. 1120–1128, 2016.

David Balduzzi and Muhammad Ghifary. Strongly-typed recurrent neural networks. In *Proceedings of The 33rd International Conference on Machine Learning*, pp. 1292–1300, 2016.

Y. Bengio, P. Simard, and P. Frasconi. Learning long-term dependencies with gradient descent is difficult. *Trans. Neur. Netw.*, 5(2):157–166, March 1994. ISSN 1045-9227. doi: 10.1109/72.279181. URL `http://dx.doi.org/10.1109/72.279181`.

Yoshua Bengio, Nicolas Boulanger-Lewandowski, and Razvan Pascanu. Advances in optimizing recurrent networks. *2013 IEEE International Conference on Acoustics, Speech and Signal Processing*, pp. 8624–8628, 2013.

James Bradbury, Stephen Merity, Caiming Xiong, and Richard Socher. Quasi-recurrent neural networks. *CoRR*, abs/1611.01576, 2016. URL `http://arxiv.org/abs/1611.01576`.

Víctor Campos, Brendan Jou, Xavier Giró-i Nieto, Jordi Torres, and Shih-Fu Chang. Skip rnn: Learning to skip state updates in recurrent neural networks. *arXiv preprint arXiv:1708.06834*, 2017.

Bo Chang, Minmin Chen, Eldad Haber, and Ed H. Chi. AntisymmetricRNN: A dynamical system view on recurrent neural networks. In *International Conference on Learning Representations*, 2019. URL `https://openreview.net/forum?id=ryxepo0cFX`.

Shiyu Chang, Yang Zhang, Wei Han, Mo Yu, Xiaoxiao Guo, Wei Tan, Xiaodong Cui, Michael Witbrock, Mark A Hasegawa-Johnson, and Thomas S Huang. Dilated recurrent neural networks. In *Advances in Neural Information Processing Systems*, pp. 77–87, 2017.

Kyunghyun Cho, Bart Van Merriënboer, Dzmitry Bahdanau, and Yoshua Bengio. On the properties of neural machine translation: Encoder-decoder approaches. *arXiv preprint arXiv:1409.1259*, 2014.

Jasmine Collins, Jascha Sohl-Dickstein, and David Sussillo. Capacity and Trainability in Recurrent Neural Networks. *arXiv e-prints*, art. arXiv:1611.09913, November 2016.

Tim Cooijmans, Nicolas Ballas, César Laurent, Çağlar Gülçehre, and Aaron Courville. Recurrent batch normalization. *arXiv preprint arXiv:1603.09025*, 2016.

Ron S Dembo, Stanley C Eisenstat, and Trond Steihaug. Inexact newton methods. *SIAM Journal on Numerical analysis*, 19(2):400–408, 1982.

Chengyue Gong, Di He, Xu Tan, Tao Qin, Liwei Wang, and Tie-Yan Liu. Frage: frequency-agnostic word representation. In *Advances in Neural Information Processing Systems*, pp. 1334–1345, 2018.

Michiel Hermans and Benjamin Schrauwen. Training and analysing deep recurrent neural networks. In C. J. C. Burges, L. Bottou, M. Welling, Z. Ghahramani, and K. Q. Weinberger (eds.), *Advances in Neural Information Processing Systems 26*, pp. 190–198. Curran Associates, Inc., 2013. URL `http://papers.nips.cc/paper/5166-training-and-analysing-deep-recurrent-neural-networks.pdf`.

Sepp Hochreiter and Jürgen Schmidhuber. Long short-term memory. *Neural computation*, 9(8): 1735–1780, 1997.

Chiori Hori, Takaaki Hori, Teng-Yok Lee, Ziming Zhang, Bret Harsham, John R Hershey, Tim K Marks, and Kazuhiko Sumi. Attention-based multimodal fusion for video description. In *ICCV*, pp. 4203–4212, 2017.

Herbert Jaeger, Mantas Lukosevicius, Dan Popovici, and Udo Siewert. Optimization and applications of echo state networks with leaky-integrator neurons. *Neural networks : the official journal of the International Neural Network Society*, 20:335–52, 05 2007. doi: 10.1016/j.neunet.2007.04.016.

Li Jing, Yichen Shen, Tena Dubcek, John Peurifoy, Scott Skirlo, Yann LeCun, Max Tegmark, and Marin Soljačić. Tunable efficient unitary neural networks (eunn) and their application to rnns. In *International Conference on Machine Learning*, pp. 1733–1741, 2017.

Diederik P. Kingma and Jimmy Ba. Adam: A method for stochastic optimization. In *ICML*, 2015.

Aditya Kusupati, Manish Singh, Kush Bhatia, Ashish Kumar, Prateek Jain, and Manik Varma. Fastgrnn: A fast, accurate, stable and tiny kilobyte sized gated recurrent neural network. In *Advances in Neural Information Processing Systems*, 2018.

Yann Lecun, Léon Bottou, Yoshua Bengio, and Patrick Haffner. Gradient-based learning applied to document recognition. In *Proceedings of the IEEE*, pp. 2278–2324, 1998.

Tao Lei, Yu Zhang, Sida I. Wang, Hui Dai, and Yoav Artzi. Simple recurrent units for highly parallelizable recurrence. In *Empirical Methods in Natural Language Processing (EMNLP)*, 2018.

James Martens and Ilya Sutskever. Learning recurrent neural networks with hessian-free optimization. In *Proceedings of the 28th International Conference on Machine Learning (ICML-11)*, pp. 1033–1040, 2011.

Zakaria Mhammedi, Andrew D. Hellicar, Ashfaqur Rahman, and James Bailey. Efficient orthogonal parametrisation of recurrent neural networks using householder reflections. *CoRR*, abs/1612.00188, 2016. URL http://arxiv.org/abs/1612.00188.

Asier Mujika, Florian Meier, and Angelika Steger. Fast-slow recurrent neural networks. In *Advances in Neural Information Processing Systems*, pp. 5915–5924, 2017.

Murphy Yuezhen Niu, Lior Horesh, and Isaac Chuang. Recurrent neural networks in the eye of differential equations. *arXiv preprint arXiv:1904.12933*, 2019.

Razvan Pascanu, Caglar Gulcehre, Kyunghyun Cho, and Yoshua Bengio. How to construct deep recurrent neural networks. *arXiv preprint arXiv:1312.6026*, 2013a.

Razvan Pascanu, Tomas Mikolov, and Yoshua Bengio. On the difficulty of training recurrent neural networks. In *International Conference on Machine Learning*, pp. 1310–1318, 2013b.

Razvan Pascanu, Çaglar Gülçehre, Kyunghyun Cho, and Yoshua Bengio. How to construct deep recurrent neural networks. *CoRR*, abs/1312.6026, 2013c.

Jeffrey Pennington, Samuel Schoenholz, and Surya Ganguli. Resurrecting the sigmoid in deep learning through dynamical isometry: theory and practice. In I. Guyon, U. V. Luxburg, S. Bengio, H. Wallach, R. Fergus, S. Vishwanathan, and R. Garnett (eds.), *Advances in Neural Information Processing Systems 30*, pp. 4785–4795. 2017.

F. Rosenblatt. *Principles of neurodynamics.* Spartan Books, Washington, D.C., 1962.

Sachin S Talathi and Aniket Vartak. Improving performance of recurrent neural network with relu nonlinearity. *arXiv preprint arXiv:1511.03771*, 2015.

Eugene Vorontsov, Chiheb Trabelsi, Samuel Kadoury, and Chris Pal. On orthogonality and learning recurrent networks with long term dependencies. In *ICML*, pp. 3570–3578, 2017. URL http://proceedings.mlr.press/v70/vorontsov17a.html.

Pete Warden. Speech Commands: A Dataset for Limited-Vocabulary Speech Recognition. *arXiv e-prints*, art. arXiv:1804.03209, April 2018.

Scott Wisdom, Thomas Powers, John Hershey, Jonathan Le Roux, and Les Atlas. Full-capacity unitary recurrent neural networks. In D. D. Lee, M. Sugiyama, U. V. Luxburg, I. Guyon, and R. Garnett (eds.), *Advances in Neural Information Processing Systems 29*, pp. 4880–4888. Curran Associates, Inc., 2016. URL http://papers.nips.cc/paper/6327-full-capacity-unitary-recurrent-neural-networks.pdf.

Inc. Yelp. Yelp dataset challenge. 2017. URL https://www.yelp.com/dataset/challenge.

Jiong Zhang, Qi Lei, and Inderjit S. Dhillon. Stabilizing gradients for deep neural networks via efficient svd parameterization. In *ICML*, 2018.

Jiong Zhang, Qi Lei, and Inderjit S Dhillon. Stabilizing gradients for deep neural networks via efficient SVD parameterization. *arXiv preprint arXiv:1803.09327*, 2018.

Julian Georg Zilly, Rupesh Kumar Srivastava, Jan Koutník, and Jürgen Schmidhuber. Recurrent highway networks. In *ICML*, pp. 4189–4198. JMLR. org, 2017.

A APPENDIX

A.1 MULTI-LAYER DEEP RNN NETWORKS.

We point out in passing that our framework readily admits deep multi-layered networks within a single time-step. Indeed our setup is general; it applies to shallow and deep nets; small and large time steps. As a case in point, the Deep Transition RNN Pascanu et al. (2013c):

$$h_{k+1} = f_h(h_k, x_{k+1}) = \phi_h(W_L \phi_{L-1}(W_{L-1} \dots W_1 \phi_1(U h_k + W x_{k+1})))$$

is readily accounted by Theorem 1 in an implicit form:

$$h_{k+1} = f_h(h_{k+1} + h_k, x_{k+1}) - h_k.$$

So is Deep-RNN Hermans & Schrauwen (2013). The trick is to transform $h_k \to h_k + h_{k+1}$ and $h_{k+1} \to h_k + h_{k+1}$. As such, all we need is smoothness of f_h, which has no restriction on # layers. On the other hand, that we do not have to limit the number of time steps is the *point* of Theorem 1, which asserts that the partial differential of hidden states (which is primarily why vanishing/exploding gradient arises Pascanu et al. (2013b) in the first place) is identity!!

A.2 CONVERGENCE GUARANTEES FOR GENERAL LEARNING RATES.

Theorem 2 (Local Convergence with Linear Rate). *Assume that the function $F(g_i) \triangleq \phi(U(g_i + h_{k-1}) + W x_k + b) - (g_i + h_{k-1})$ and the parameter $\eta_k^{(i)}$ in Eq. 5 satisfies*

$$[\eta_k^{(i)}]^2 \|\nabla F(g_i) F(g_i)\|^2 + 2\eta_k^{(i)} F(g_i)^\top \nabla F(g_i) F(g_i) < 0, \forall k, \forall i. \tag{9}$$

Then there exists $\epsilon > 0$ such that if $\|g_0 - h_{eq}\| \leq \epsilon$ where h_{eq} denotes the fixed point, the sequence g_i generated by the Euler method converges to the equilibrium solution in $\mathcal{M}_{eq}(h_{k-1}, x_k)$ locally with linear rate.

The proof is based on drawing a connection between the Euler method and inexact Newton methods, and leverages Thm. 2.3 in Dembo et al. (1982). See appendix Sec. A.7.1 Thm. 3 and Sec. A.6.5 (for proof, empirical verification).

Corollary 1. *If $\|\mathbf{I} + \eta_k^{(i)} \nabla F(g_i)\| < 1, \forall k, \forall i$, the forward propagation (Eq. 12) is stable and the sequence $\{g_i\}$ converges locally at a linear rate.*

The proof is based on Thm. 2.3 in Dembo et al. (1982), Thm. 2 and Prop. 2 in Chang et al. (2019). See appendix A.7.1 Corollary. 2

Table 4: Dataset Statistics & Long Term Dependence

Dataset	Avg. Activity Time	Input Time	Sequence Ratio	#Train	#Fts	#Steps	#Test
Google-30	25ms	1000ms	3/99	51,088	32	99	6,835
HAR-2	256ms	2560ms	13/128	7,352	9	128	2,947
Noisy-MNIST	28	1000	7/250	60,000	28	1000	10,000
Noisy-CIFAR	32	1000	4/125	60,000	96	1000	10,000
Pixel-MNIST				60,000	1	784	10,000
Permuted-MNIST				60,000	1	784	10,000

A.3 DATASET DETAILS

Table 4 and table 6 lists the statistics of all the datasets described below.

Google-12 & Google-30: Google Speech Commands dataset contains 1 second long utterances of 30 short words (30 classes) sampled at 16KHz. Standard log Mel-filter-bank featurization with 32 filters over a window size of 25ms and stride of 10ms gave 99 timesteps of 32 filter responses for a 1-second audio clip. For the 12 class version, 10 classes used in Kaggle's Tensorflow Speech Recognition challenge[8] were used and remaining two classes were noise and background sounds (taken randomly from remaining 20 short word utterances). Both the datasets were zero mean - unit variance normalized during training and prediction.

HAR-2[9]: Human Activity Recognition (HAR) dataset was collected from an accelerometer and gyroscope on a Samsung Galaxy S3 smartphone. The features available on the repository were directly used for experiments. The 6 activities were merged to get the binarized version. The classes Sitting, Laying, Walking_Upstairs and Standing, Walking, Walking_Downstairs were merged to obtain the two classes. The dataset was zero mean - unit variance normalized during training and prediction.

Penn Treebank: 300 length word sequences were used for word level language modeling task using Penn Treebank (PTB) corpus. The vocabulary consisted of 10,000 words and the size of trainable word embeddings was kept the same as the number of hidden units of architecture. This is the setup used in (Kusupati et al., 2018; Zhang et al., 2018).

Pixel-MNIST: Pixel-by-pixel version of the standard MNIST-10 dataset [10]. The dataset was zero mean - unit variance normalized during training and prediction.

Permuted-MNIST: This is similar to Pixel-MNIST, except its made harder by shuffling the pixels with a fixed permutation. We keep the random seed as 42 to generate the permutation of 784 pixels.

Noisy-MNIST: To introduce more long-range dependencies to the Pixel-MNIST task, we define a more challenging task called the Noisy-MNIST, inspired by the noise padded experiments in Chang et al. (2019). Instead of feeding in one pixel at one time, we input each row of a MNIST image at every time step. After the first 28 time steps, we input independent standard Gaussian noise for the remaining time steps. Since a MNIST image is of size 28 with 1 RGB channels, the input dimension is m = 28. The total number of time steps is set to T = 1000. In other words, only the first 28 time steps of input contain salient information, all remaining 972 time steps are merely random noise. For a model to correctly classify an input image, it has to remember the information from a long time ago. This task is conceptually more difficult than the pixel-by-pixel MNIST, although the total amount of signal in the input sequence is the same.

Noisy-CIFAR: This is exactly replica of the noise paded CIFAR task mentioned in Chang et al. (2019). Instead of feeding in one pixel at one time, we input each row of a CIFAR-10 image at every time step. After the first 32 time steps, we input independent standard Gaussian noise for the remaining time steps. Since a CIFAR-10 image is of size 32 with three RGB channels, the input dimension is m = 96. The total number of time steps is set to T = 1000. In other words, only the first

---

[8]https://www.kaggle.com/c/tensorflow-speech- recognition-challenge

[9]https://archive.ics.uci.edu/ml/datasets/human+activity+recognition+using+ smartphones

[10]http://yann.lecun. com/exdb/mnist/

32 time steps of input contain salient information, all remaining 968 time steps are merely random noise. For a model to correctly classify an input image, it has to remember the information from a long time ago. This task is conceptually more difficult than the pixel-by-pixel CIFAR-10, although the total amount of signal in the input sequence is the same.

Addition Task: We closely follow the adding problem defined in (Arjovsky et al., 2016; Hochreiter & Schmidhuber, 1997) to explain the task at hand. Each input consists of two sequences of length T. The first sequence, which we denote x, consists of numbers sampled uniformly at random $\mathcal{U}[0, 1]$. The second sequence is an indicator sequence consisting of exactly two entries of 1 and remaining entries 0. The first 1 entry is located uniformly at random in the first half of the sequence, whilst the second 1 entry is located uniformly at random in the second half. The output is the sum of the two entries of the first sequence, corresponding to where the 1 entries are located in the second sequence. A naive strategy of predicting 1 as the output regardless of the input sequence gives an expected mean squared error of 0.167, the variance of the sum of two independent uniform distributions.

Copying Task: Following a similar setup to (Arjovsky et al., 2016; Hochreiter & Schmidhuber, 1997), we outline the copy memory task. Consider 10 categories, $\{a_i\}_{i=0}^9$. The input takes the form of a $T + 20$ length vector of categories, where we test over a range of values of T. The first 10 entries are sampled uniformly, independently and with replacement from $\{a_i\}_{i=0}^7$, and represent the sequence which will need to be remembered. The next $T - 1$ entries are set to a_8, which can be thought of as the 'blank' category. The next single entry is a_9, which represents a delimiter, which should indicate to the algorithm that it is now required to reproduce the initial 10 categories in the output. The remaining 10 entries are set to a_8. The required output sequence consists of $T + 10$ repeated entries of a_8, followed by the first 10 categories of the input sequence in exactly the same order. The goal is to minimize the average cross entropy of category predictions at each time step of the sequence. The task amounts to having to remember a categorical sequence of length 10, for T time steps.

A simple baseline can be established by considering an optimal strategy when no memory is available, which we deem the memoryless strategy. The memoryless strategy would be to predict a_8 for $T + 10$ entries and then predict each of the final 10 categories from the set $\{a_i\}_{i=0}^7$ i=0 independently and uniformly at random. The categorical cross entropy of this strategy is $\frac{10 \log(8)}{T+20}$

DSA-19[11]: This dataset is based on Daily and Sports Activity (DSA) detection from a resource-constrained IoT wearable device with 5 Xsens MTx sensors having accelerometers, gyroscopes and magnetometers on the torso and four limbs. The features available on the repository were used for experiments. The dataset was zero mean - unit variance normalized during training and prediction.

Yelp-5: Sentiment Classification dataset based on the text reviews[12]. The data consists of 500,000 train points and 500,000 test points from the first 1 million reviews. Each review was clipped or padded to be 300 words long. The vocabulary consisted of 20000 words and 128 dimensional word embeddings were jointly trained with the network.

A.4 BASELINE JUSTIFICATION

In our experiments section, we stated that some of the potential baselines were removed due to experimental conditions enforced in the setup. Here we clearly justify our choice. Mostly the reasoning is to avoid comparing complementary add-ons and compare the bare-bone cells.

- Cooijmans et al. (2016) is removed since its an add-on and can be applied to any method. Besides its pixel-mnist results involve dataset specific heuristics.
- Gong et al. (2018) is also an add-on and hence can be applied to any method.
- Zilly et al. (2017); Pascanu et al. (2013a); Mujika et al. (2017) denote deep transitioning methods. They are add-ons for any single recurrent block and hence can be applied to any recurrent cell.
- Gating variants of single recurrent cells (Chang et al., 2019; Kusupati et al., 2018) have also been removed. Since *iRNN* can be extended to a gating variant and hence its just an add-on.

---

[11]https://archive.ics.uci.edu/ml/datasets/Daily+and+Sports+Activities
[12]https://www.yelp.com/dataset/challenge

Table 5: Various hyper-parameters to reproduce results

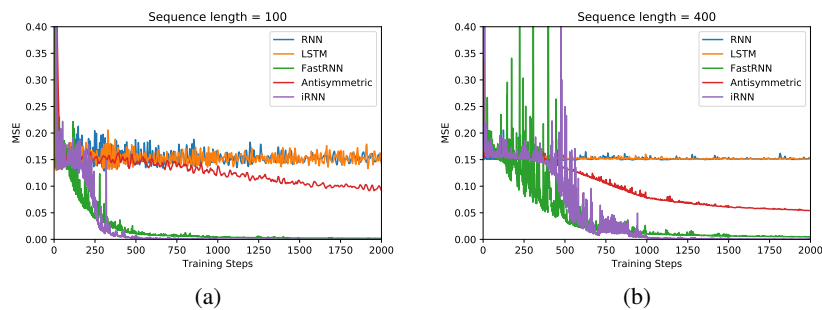| Dataset	Hidden Units
Google-30	80
HAR-2	80
Pixel-MNIST	128
Permuted-MNIST	128
Noisy-MNIST	128
Noisy-CIFAR	128
Addition Task	128
Copying Task	128
PTB	256

Figure 5: Mean Squared Error shown for the Add Task (Sequence Length) : (c) 100 (d) 400

A.5 HYPER-PARAMETERS FOR REPRODUCIBILITY

We report various hyper-parameters we use in our experiments for reproduciblity. As mentioned earlier we mainly use 'ReLU' as the non-linearity and Adam as the optimizer. Apart from this, other hyper-parameters are mentioned in table 5.

A.6 ADDITIONAL EXPERIMENTS

Table 6: Other Dataset Statistics & Long Term Dependence

Dataset	Avg. Acitivity Time	Input Time	Sequence Ratio	#Train	#Fts	#Steps	#Test
Google-12	25ms	1000ms	3/99	22,246	32	99	3,081
DSA-19	500ms	5000ms	13/125	4,560	45	125	4,560
Yelp-5	20	300	1/15	500,000	128	300	500,000
PTB				929,589	300	300	82,430

A.6.1 COPYING AND ADDITION TASKS

Figure 5 shows the results for remaining experiments for the addition task for length 100, 400.

A.6.2 TRADITIONAL DATASETS

Table 7 shows the results including left out baselines for Pixel-MNIST and permute-MNIST task. Here we also include star rating prediction on a scale of 1 to 5 of Yelp reviews Yelp (2017). Table 8 shows the results for this dataset.

Table 7: Results for Pixel-by-Pixel MNIST and Permuted MNIST datasets. K denotes pre-defined recursions embedded in graph to reach equillibrium.

Data set	Algorithm	Accuracy (%)	Train Time (hr)	#Params
Pixel-MNIST	FastRNN	96.44	15.10	33k
	FastGRNN-LSQ	**98.72**	12.57	14k
	RNN	94.10	45.56	14k
	SpectralRNN	97.7		6k
	LSTM	97.81	26.57	53k
	URNN	95.1		16k
	Antisymmetric	98.01	8.61	14k
	iRNN (K=1)	97.73	**2.83**	**4k**
	iRNN (K=2)	98.13	3.11	**4k**
	***iRNN* (K=3)**	98.13	2.93	**4k**
Permute-MNIST	FastRNN	92.68	9.32	8.75k
	SpectralRNN	92.7		8.5k
	LSTM	92.61	19.31	35k
	URNN	91.4		12k
	Antisymmetric	93.59	4.75	14k
	***iRNN* (K=1)**	**95.62**	**2.41**	**8k**

Table 8: Results for Yelp Dataset.

Data set	Algorithm	Accuracy (%)	Model Size (KB)	Train Time (hr)	Test Time (ms)	#Params
Yelp-5	FastRNN	55.38	130	3.61	**0.4**	32.5k
	FastGRNN-LSQ	**59.51**	130	3.91	0.7	32.5k
	FastGRNN	59.43	8	4.62		
	RNN	47.59	130	3.33	**0.4**	32.5k
	SpectralRNN	56.56	**89**	4.92	0.3	**22k**
	EURNN	59.01	122	72.00		
	LSTM	59.49	516	8.61	1.2	129k
	GRU	59.02	388	8.12	0.8	97k
	Antisymmetric	54.14	130	2.61	**0.4**	32.5k
	UGRNN	58.67	258	4.34		
	iRNN (K=1)	58.16	97.67	**0.31**	**0.4**	25k
	iRNN (K=2)	59.01	98.84	**0.31**	0.7	25k
	iRNN (K=3)	59.34	100	1.16	1.0	25k

A.6.3 ACTIVITY RECOGNITION DATASETS

We also include activity recognition tasks: (a)Google-12 Warden (2018) , *i.e.* detection of utterances of 10 commands plus background noise and silence and (b) DSA-19 Altun et al. (2010), Daily and Sports Activity (DSA) detection from a resource-constrained IoT wearable device with 5 Xsens MTx sensors having accelerometers, gyroscopes and magnetometers on the torso and four limbs. Table 9 shows results for these activities along with some other baselines for activity recognition tasks mentioned in Sec. 4.3.4 and described in Sec. A.3.

A.6.4 PTB LANGUAGE MODELLING

We follow (Kusupati et al., 2018; Zhang et al., 2018) to setup our PTB experiments. We only pursue one layer language modelling, but with more difficult sequence length (300). Table 10 reports all the evaluation metrics for the PTB Language modelling task with 1 layer as setup by Kusupati et al. (2018), including test time and number of parameters (which we omitted from the main paper due to lack of space).

A.6.5 Linear Rate of Convergence to Fixed Poi

Empirically we verify the local convergence to a fixed point with linear rate by comparing the Euclidean distance between the approximate solutions, $\mathbf{h}_t^{(k)}$, using Eq. 10 with $g_0 = 0$ and the fixed points, $\mathbf{h}_t$, computed using FSOLVE from SCIPY. The learnable parameters are initialized suitably and then fixed. We illustrate our results in Fig. 6, which clearly demonstrates that the approximate solutions tend to converge with linear rate.
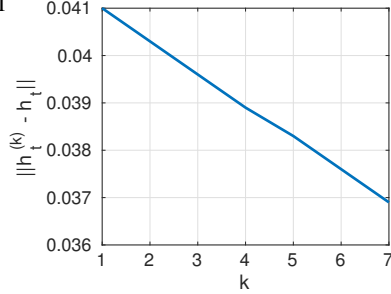

Figure 6: Linear convergence in *iRNN* .

$$g_i = g_{i-1} + \eta_t^i(\phi(U(g_{i-1} + h_{t-1}) + W x_t + b) - \alpha(g_{i-1} + h_{t-1})) \tag{10}$$
$$h_t^K = g_K$$

A.6.6 Theoretical Verification

Here we include some experiments to show that our theoretical assumptions hold true.
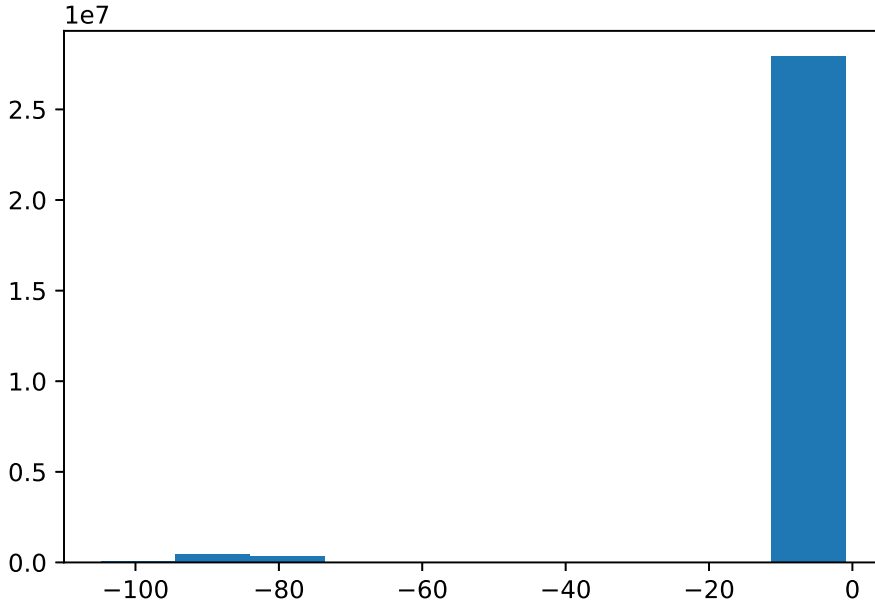

Figure 7: Histogram of the eigenvalues of $\nabla\phi\mathbf{U} - \mathbf{I}$ for *iRNN* on HAR-2 dataset.

Non-Singularity of the matrix D For our *iRNN* parametrization to satisfy the conditions of having equillibrium points to be locally asymptotically stable, the eigen values of the matrix $D = (\nabla\phi(\cdot)U - \gamma I)$ should be negative. We plot a histogram of the eigenvalues of D for all the points in the HAR-2 dataset. As illustrated in the figure 7, all the eigenvalues are negative.

A.6.7 Identity Gradient comparison *iRNN* vs RNN

To verify Theorem. 1 empirically, we train RNN and iRNN on the HAR-2 data set (see more details in Sec. 4), respectively, and plot in Fig. 8 the magnitude of gradient of the last layer $\mathbf{h}_T$ *w.r.t.* the first layer $\mathbf{h}_1$ in log scale to confirm that our approach leads to no vanishing or exploding gradients when the error is back-propagated through time. We also conducted experiments to verify that the gradient of iRNN is norm preserving (see Sec. A.6.8 and Figure . 3). As we see clearly, RNN suffers from
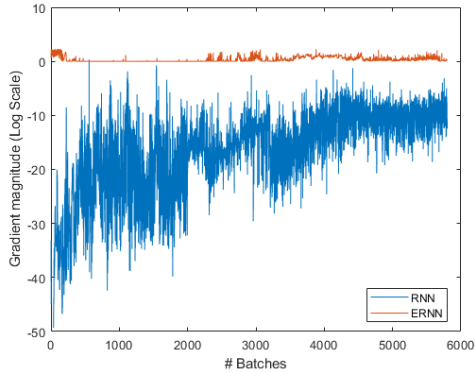
(a)

Figure 8: Comparison between RNN and iRNN on the magnitudes of gradients.

serious vanishing gradient issue in training, while iRNN's backpropagated gradients is close to 1, and the variance arises mainly our approximation of fixed points and stochastic behavior in training networks, demonstrating much better training stability of iRNN.

A.6.8 Gradient norm w.r.t. loss $\|\frac{\partial L}{\partial h_1}\|$

In addition to the gradient ratio we plot in Sec.4.2, we also show in figure 9, the more popular quantity captured in earlier works (Arjovsky et al., 2016; Zhang et al., 2018), i.e. the gradient norm w.r.t. loss $\|\frac{\partial L}{\partial h_1}\|$. We emphasize that this quantity alone is misleading in the context of resolving the issue of vanishing/exploding gradients. Since $\|\frac{\partial L}{\partial h_1}\| = \|\frac{\partial L}{\partial h_T}\| * \|\frac{\partial h_T}{\partial h_1}\|$. The long term component controlling the gradients is $\|\frac{\partial h_T}{\partial h_1}\|$, but the other component, $\|\frac{\partial L}{\partial h_T}\|$ could become zero by the virtue that the loss is nearly zero. This happens in our addition task experiment, because MSE is close to zero, we experience nearly 0 value for this quantity. But this is clearly because the MSE is 0. Also note that none of our graphs have log scale, which is not the case in earlier works. The conclusion that can be drawn from the loss-gradient is that it is somewhat stable, and can inform us about quality of convergence.

We also plot $\|\frac{\partial h_T}{\partial h_{T-1}}\|$ in figure 9 in order to show that indeed *iRNN* achieves identity gradients everywhere in the time horizon, since fig. 3 had shown that the ratio of $\|\frac{\partial h_T}{\partial h_1}\|$ and $\|\frac{\partial h_T}{\partial h_{T-1}}\|$ equals 1 for *iRNN* .

A.6.9 Different Activation Function

We also performed some experiments for sigmoid activation on HAR-2 dataset. The results for this variant also follow similar pattern as we saw in ReLU variant.

A.7 Proofs

A.7.1 Local Convergence with Linear Rate

Recall that we rewrite the fixed-point constraints in our *iRNN* as the following ODE:

$$g_k'(t) = F(g_i) \overset{def}{=} \phi(U(g_i + h_{k-1}) + W x_k + b) - (g_i + h_{k-1}); \; g(0) = 0. \qquad (11)$$

Then based on the Euler method, we have the following update rule for solving fixed-points:

$$g_{i+1} = g_i + \eta_k^{(i)} F(g_i) \qquad (12)$$

$$= g_i + \eta_k^{(i)}[\phi(U(g_i + h_{k-1}) + W x_k + b) - (g_i + h_{k-1})]. \qquad (13)$$
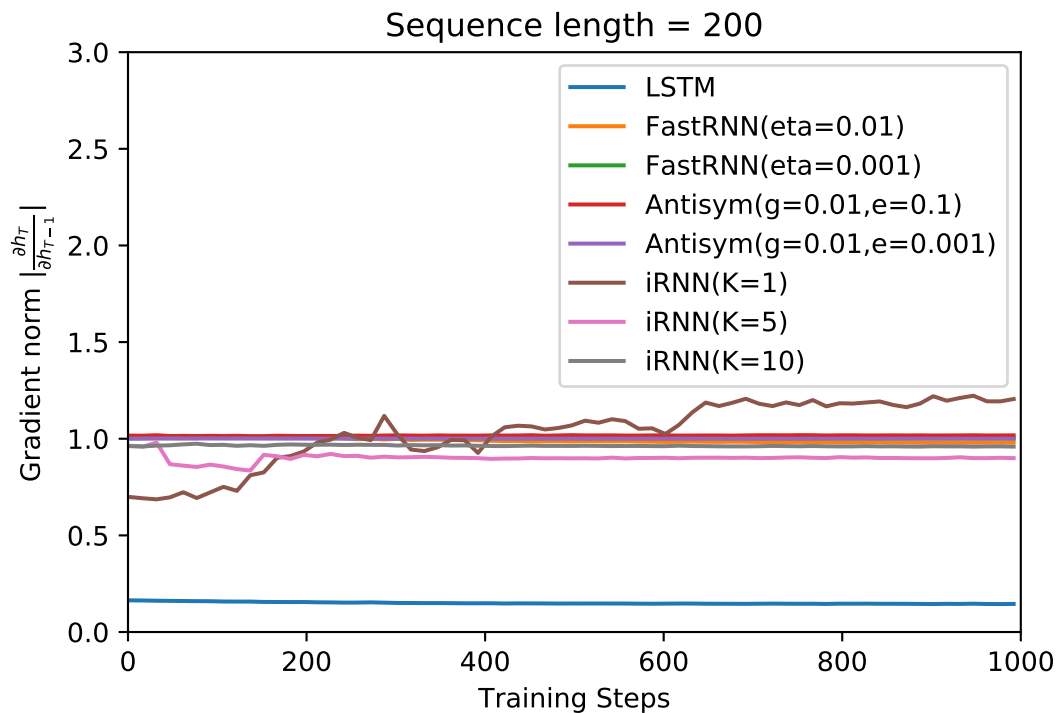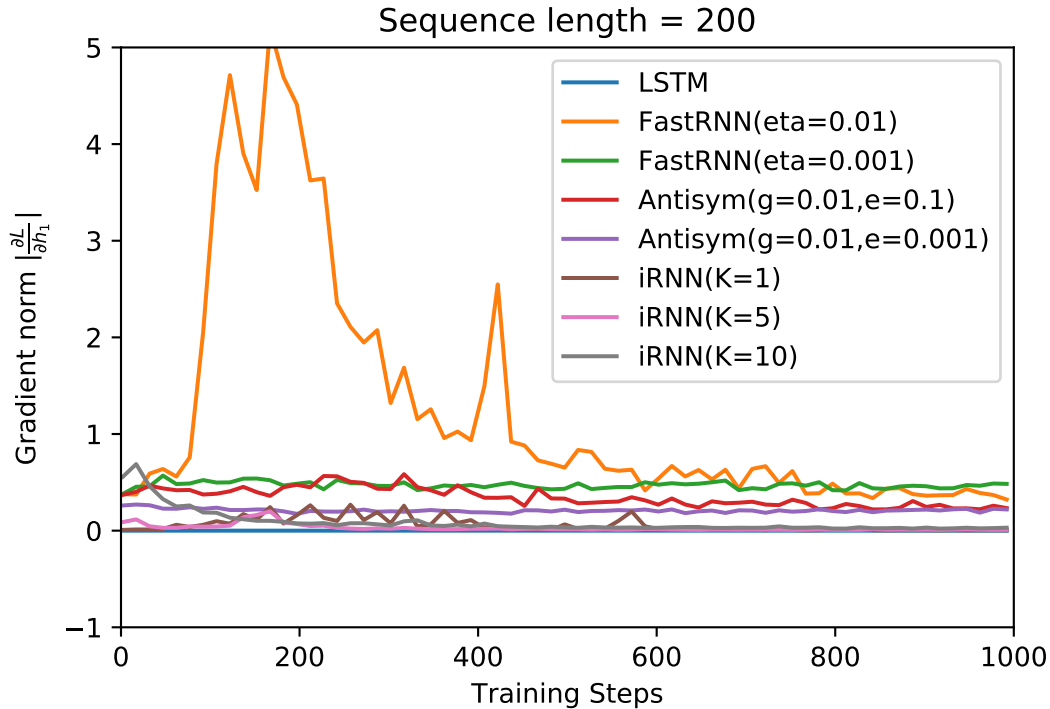
(a)

(b)

Figure 9: Exploratory experiments for the Add task : (a) Gradient norms w.r.t. loss $\|\frac{\partial L}{\partial h_1}\|$, (b) Gradient norms $\|\frac{\partial h_T}{\partial h_{T-1}}\|$. This together with Figure 3 shows that the gradients are identity everywhere for $K = 10$

Inexact Newton methods Dembo et al. (1982) refer to a family of algorithms that aim to solve the equation system $F(z) = 0$ approximately at each iteration using the following rule:

$$z_{i+1} = z_i + s_i, \ r_i = F(z_i) + \nabla F(z_i)s_i, \tag{14}$$

where ∇F denotes the (sub)gradient of function F, and r_i denotes the error at the i-th iteration between $F(z_i)$ and 0.

By drawing the connection between Eq. 12 and Eq. 14, we can set $z_i \equiv g_i$ and $s_i \equiv \eta_k^{(i)} F(g_i)$. Then based on Eq. 14 we have

$$r_i = F(g_i) + \eta_k^{(i)} \nabla F(g_i) F(g_i). \tag{15}$$

Lemma 1 (Thm. 2.3 in Dembo et al. (1982)). *Assume that*

$$\frac{\|r_i\|}{\|F(z_i)\|} \leq \tau < 1, \forall k, \tag{16}$$

where $\| \cdot \|$ denotes an arbitrary norm and the induced operator norm. There exists $\varepsilon > 0$ such that, if $\|z_0 - z_*\| \leq \varepsilon$, then the sequence of inexact Newton iterates $\{z_i\}$ converges to z_*. Moreover, the convergence is linear in the sense that $\|z_{i+1} - z_*\|_* \leq \tau \|z_i - z_*\|_*$, where $\|y\|_* = \|\nabla F(z_*)y\|$.

Theorem 3 (Local Convergence with Linear Rate). *Assume that the function F in Eq. 11 and the parameter $\eta_k^{(i)}$ in Eq. 12 satisfy*

$$[\eta_k^{(i)}]^2 \|\nabla F(g_i)F(g_i)\|^2 + 2\eta_k^{(i)} F(g_i)^\top \nabla F(g_i) F(g_i) < 0, \forall i, \forall k. \tag{17}$$

Then there exists $\epsilon > 0$ such that if $\|g_0 - h_{eq}\| \leq \epsilon$ where h_{eq} denotes the fixed point, the sequence $\{g_i\}$ generated by the Euler method converges to the equilibrium solution in $\mathcal{M}_{eq}(h_{k-1}, x_k)$ locally with linear rate.

Proof. By substituting Eq. 15 into Eq. 16, to prove local convergence we need to guarantee

$$\|F(g_i) + \eta_k^{(i)} \nabla F(g_i) F(g_i)\| < \|F(g_i)\|. \tag{18}$$

By taking the square of both sides in Eq. 18, we can show that Eq. 18 is equivalent to Eq. 17. We then complete our proof.

$\square$

Corollary 2. *Assume that $\|\mathbf{I} + \eta_k^{(i)} \nabla F(g_i)\| < 1, \forall i, \forall k$ holds. Then the forward propagation using Eq. 12 is stable and our sequence $\{g_i\}$ converges locally with linear rate.*

Proof. By substituting Eq. 15 into Eq. 16 and based on the assumption in the corollary, we have

$$\begin{aligned}
\frac{\|r_i\|}{\|F(g_i)\|} &= \frac{\|F(g_i) + \eta_k^{(i)} \nabla F(g_i) F(g_i)\|}{\|F(g_i)\|} \\
&\leq \frac{\|\mathbf{I} + \eta_k^{(i)} \nabla F(g_i)\| \|F(g_i)\|}{\|F(g_i)\|} < 1.
\end{aligned} \tag{19}$$

Further based on Prop. 2 in Chang et al. (2019) and Thm. 2, we then complete our proof. $\square$

Table 9: Results for Activity Recoginition Datasets.

Data set	Algorithm	Accuracy (%)	Model Size (KB)	Train Time (hr)	Test Time (ms)	#Params
HAR-2	FastRNN	94.50	29	0.063	**0.01**	7.5k
	FastGRNN-LSQ	95.38	29	0.081	0.03	7.5k
	FastGRNN	95.59	3	0.10		
	RNN	91.31	29	0.114	**0.01**	7.5k
	SpectralRNN	95.48	525	0.730	0.04	134k
	EURNN	93.11	**12**	0.740		
	LSTM	93.65	74	0.183	0.04	16k
	GRU	93.62	71	0.130	0.02	16k
	Antisymmetric	93.15	29	0.087	**0.01**	7.5k
	UGRNN	94.53	37	0.120		
	iRNN (K=1)	95.32	**17**	0.061	**0.01**	**4k**
	iRNN (K=3)	95.52	**17**	0.081	0.02	**4k**
	iRNN (K=5)	**96.30**	18	**0.018**	0.03	**4k**
DSA-19	FastRNN	84.14	97	0.032	**0.01**	17.5k
	FastGRNN-LSQ	85.00	208	0.036	0.03	35k
	FastGRNN	83.73	3.25	2.10m		
	RNN	71.68	20	0.019	**0.01**	**3.5k**
	SpectralRNN	80.37	50	0.038	0.02	8.8k
	LSTM	84.84	526	0.043	0.06	92k
	GRU	84.84	270	0.039	0.03	47k
	Antisymmetric	85.37	32	0.031	**0.01**	8.3k
	UGRNN	84.74	399	0.039		
	iRNN (K=1)	**88.11**	**19**	0.015	**0.01**	**3.5k**
	iRNN (K=3)	85.20	**19**	0.020	0.02	**3.5k**
	iRNN (K=5)	87.37	20	**0.005**	0.03	**3.5k**
Google-12	FastRNN	92.21	56	0.61	**0.01**	12k
	FastGRNN-LSQ	93.18	57	0.63	0.03	12k
	FastGRNN	92.10	5.5	0.75		
	RNN	73.25	56	1.11	**0.01**	12k
	SpectralRNN	91.59	228	19.0	0.05	49k
	EURNN	76.79	210	120.00		
	LSTM	92.30	212	1.36	0.05	45k
	GRU	93.15	248	1.23	0.05	53k
	Antisymmetric	89.91	57	0.71	**0.01**	12k
	UGRNN	92.63	75	0.78		
	iRNN (K=1)	93.93	**36**	0.20	**0.01**	**8.1k**
	iRNN (K=3)	94.16	37	0.33	0.03	**8.1k**
	iRNN (K=5)	**94.71**	38	**0.17**	0.05	**8.1k**
Google-30	FastRNN	91.60	96	1.30	**0.01**	18k
	FastGRNN-LSQ	92.03	45	1.41	**0.01**	**8.5k**
	FastGRNN	90.78	6.25	1.77		
	RNN	80.05	63	2.13	**0.01**	12k
	SpectralRNN	88.73	128	11.0	0.03	24k
	EURNN	56.35	135	19.00		
	LSTM	90.31	219	2.63	0.05	41k
	GRU	91.41	257	2.70	0.05	48.5k
	Antisymmetric	90.91	64	0.54	**0.01**	12k
	UGRNN	90.54	260	2.11		
	iRNN (K=1)	93.77	**44**	0.44	**0.01**	**8.5k**
	iRNN (K=3)	91.30	**44**	0.44	0.03	**8.5k**
	iRNN (K=5)	**94.23**	45	**0.44**	0.05	**8.5k**

Algorithm	Test Perplexity	Model Size (KB)	Train Time (min)	Test Time (ms)	#Params
FastRNN	127.76	513	11.20	1.2	52.5k
FastGRNN-LSQ	115.92	513	12.53	1.5	52.5k
FastGRNN	116.11	39	13.75		
RNN	144.71	**129**	9.11	**0.3**	**13.2k**
SpectralRNN	130.20	242	-	0.6	24.8k
LSTM	117.41	2052	13.52	4.8	210k
UGRNN	119.71	256	11.12	0.6	26.3k
iRNN (**K=1**)	**115.71**	288	**7.11**	0.6	29.5k

Table 10: PTB Language Modeling: 1 Layer. To be consistent with our other experiments we used a low-dim $\mathbf{U}$; For this size our results did not significantly improve with K. This is the dataset of Kusupati et al. (2018) which uses sequence length 300 as opposed to 30 in the conventional PTB.

Data set	Algorithm	Accuracy (%)	Model Size (KB)	Train Time (hr)	Activation	#Params
HAR-2	*iRNN* (K=1)	95.32	**17**	0.061	ReLU	**4k**
	iRNN (K=3)	95.52	**17**	0.081	ReLU	**4k**
	***iRNN* (K=5)**	**96.30**	18	**0.018**	ReLU	**4k**
	iRNN (K=1)	92.16	**17**	0.065	Sigmoid	**4k**
	iRNN (K=3)	93.35	**17**	0.078	Sigmoid	**4k**
	***iRNN* (K=5)**	95.30	18	0.020	Sigmoid	**4k**

Table 11: HAR-2 dataset (Sigmoid, ReLU activations): K denotes pre-defined recursions embedded in graph to reach equillibrium.